J Mater Sci (2018) 53:3341–3363

Chemical routes to materials

Preparation and characterization of photocatalytic TiO_2 films on functionalized stainless steel

Nesrine Barbana[1], Adel Ben Youssef[1,2], Hafedh Dhiflaoui[2], and Latifa Bousselmi[1,*]

[1] *Center of Water Research and Technologies, Technopark of Borj-Cedria, PO-box No 273 - 8020, Soliman, Tunisia*
[2] *National High School of Engineers of Tunisia, University of Tunis, 5 Taha Hussein Street, 1008 Tunis, Tunisia*

Received: 15 June 2017
Accepted: 24 October 2017

ABSTRACT

In this study, TiO_2 was synthesized using controlled hydrolysis of $TiCl_4$, followed by dialysis. We produced a transparent emulsion that was later dried into TiO_2 powder. TiO_2 photocatalyst films were deposited applying the technique of pulsed electrophoretic deposition, which decreased bubble formation caused by direct current. The substrates were bare stainless steel (SS) and stainless steel pre-functionalized in a conversion bath. Film surface morphology, crystallinity, elemental composition, and wettability were determined using XRD, SEM–EDAX, and contact angle measurements. The mechanical properties were determined by nano-indentation test. The adhesion was investigated using scratch test. The obtained results showed that the TiO_2 film over a conversion layer had better adhesion and mechanical properties than TiO_2 over bare SS. The optical characteristics of TiO_2 films were tested using PL measurement. The photocatalytic decolourization of the amido black-10B dye was studied over TiO_2 coating under UV and visible light irradiation. TiO_2 film over a conversion layer without heat treatment exhibited the best photocatalytic activity as a result of its crystalline size and three-phase structure as well as the synergetic effect of TiO_2 and Fe_2O_3.

Abbreviations

PL	Photoluminescence
W_B	Brookite mass fraction
W_R	Rutile mass fraction
W_A	Anatase mass fraction
D_B	Brookite diameter
D_R	Rutile diameter
D_A	Anatase diameter
COD	Chemical oxygen demand
AB-10B	Amido black-10B
A_A	Anatase intensity
A_B	Brookite intensity
AB	Amido black
E	Young's modulus
H	Hardness
SS	Stainless steel
CL	Conversion layer
DC	Direct current

Address correspondence to E-mail: latifa.bousselmi@certe.rnrt.tn

https://doi.org/10.1007/s10853-017-1755-5

L_C	Load charge
EPD	Electrophoretic deposition
Pulsed EPD	Pulsed electrophoretic deposition
A_R	Rutile intensity

Introduction

Synthetic dyes have been intensively used during the last few decades. They are the most persistent pollutants, especially in industrial wastewaters. Therefore, the expansion of dye elimination research is an important topic endorsing the search for original methods to protect the environment from the aggressive effect of recalcitrant pollutants. In addition, the photocatalytic degradation of organic pollutants in water using semiconductors has been widely studied [1].

The great versatility of TiO_2 is due to its high photocatalytic activity, chemical stability, low cost, and non-toxicity [2–7]. It covers various fields, such as water purification, air depollution, and solar energy conversion. In fact, several researchers investigated the fixation of TiO_2 for water depollution in order to remove any separation step of the photocatalyst from the treated water.

TiO_2 layers on metallic surfaces can be formed employing diverse methods, such as cyclic voltammetry electrodeposition [8], anodization [9], spray plasma technique [10], sol–gel [11], and electrophoretic deposition (EPD), which could provide uniform thin films [12–21]. Indeed, few studies were reported on the EPD of TiO_2 nanoparticles by organic suspensions [22–25] or mixtures of organic solvents and water [1, 26–29]. At low voltages, the electrophoresis of TiO_2 nanoparticles is generally realized using ethanol–water mixtures without stabilizers addition [1] or by adding compounds such as $(C_2H_5)_4NOH$ and Tiron molecule [26, 27].

Employing aqueous medium without adding organic solvents was studied in few previous works as [16] where EPD was performed by suspensions of commercial TiO_2 nano-powder (Degussa P25). The use of aqueous medium can lead to bubble formation in the deposit. To overcome this problem without modifying the EPD process, pulsed voltage was used instead of direct voltage. This method is an interesting process employed to deposit a controlled coating over different conductive substrates by adjusting the deposition parameters, such as the applied voltage, the deposition time, the applied frequency, the duty cycle, and the suspension concentration.

Stainless steel (SS) has also been applied to develop TiO_2 films [29–32] due to its electrical properties. In addition, it has been extensively used in various industrial applications.

Yet, the deposition of coatings over bare SS may present a low adhesion [14, 33]. Thus, several adjustment procedures were introduced to adapt the surface of SS. Because the choice of the interlayer material needs previous knowledge about the application field, a conversion layer (CL) should be developed before the coating deposition.

In this context, this paper presents an innovative approach for the production of TiO_2 nanoparticles and their deposition on SS surface. Pulsed electrophoretic deposition of TiO_2 coating was applied over the treated SS substrates. The conversion layer has high surface area and a remarkable morphology with microspores and large cavities [34]. These properties help enhance the TiO_2 film adherence. Furthermore, the synergy between Fe_2O_3 and TiO_2 enhances the photocatalytic treatment efficiency by acting on charges recombination. Because the TiO_2 film crystalline structure, its morphology, and its particle size can affect its photocatalytic efficiency [35], the produced film was studied, in this research work, before and after calcination.

Materials and methods

Preparation of the TiO_2 thin films

To have an efficient and moderate hydrolysis, 20 ml titanium tetrachloride ($TiCl_4$, 98%, Sigma-Aldrich) was gradually dropped into 200 ml of ice-deionized water under continuous stirring until the white fog disappeared [36, 37]. Because of the extremely exothermic reaction, the solution temperature became rapidly hot. In order to eliminate the large amount of chloride ions in the system, the prepared solution was dialyzed using a Nadir®-Dialysis Tubing Membrane.

The produced titanium hydroxide/hydrous titanium oxide ($TiO_2{\cdot}nH_2O$) was transparent like soft gel. It was subsequently dried at 120 °C for 6 h. The aggregate dry TiO_2 powder was manually ground in a mortar for 15 min until obtaining a fine white

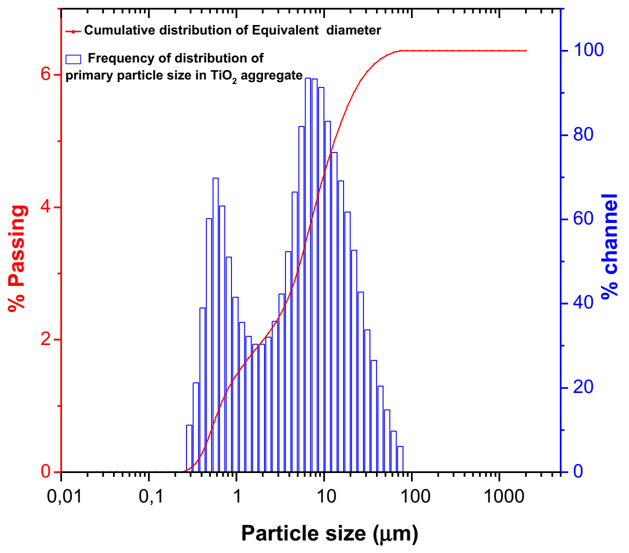

Figure 1 Grain size frequency histogram for a synthesized TiO_2 analyzed by laser granulometer.

powder. TiO_2 particles had an average particle size < 80µm as revealed in Fig. 1. The particles of synthesized TiO_2 were analyzed by laser diffraction method. The TiO_2 grains had a wide range of size distribution ranging from 0.2 to 80 µm. The histogram in Fig. 1 illustrates two peaks corresponding to two average sizes of aggregates. The first one corresponds to 75% of the total volume with a diameter of 7.76 µm, while the second one represents 25% and has a diameter of 0.57 µm.

A suspension of 10 g/l concentration was made by mixing TiO_2 nanoparticles and deionized water in a glass beaker. It was magnetically stirred for 30 min. This suspension was used to deposit TiO_2 over both bare SS 316L and a pre-functionalized steel with a CL. The working electrode disks of 15 mm diameter and 0.8 mm thickness were mechanically polished using SiC papers in a sequence of 400, 600, 800, and 1200. They were cleaned using deionized water. Then, they were dried at ambient temperature.

The conversion coatings were prepared on SS disks by an oxidation in a conversion bath composed of 5 ml of sulfuric acid mixed with 0.126 g of hydrated sodium thiosulfate and 0.6 ml of propargylic alcohol in a 100-ml volumetric flask [34]. The immersion period of the sample in the conversion bath was 35 min at a temperature between 60 and 70 °C. The prepared samples were rinsed in demineralized water. Then, they were dried at 120 °C for 60 min. After that, the layers were subject to heat treatment at 450 °C for 2 h to achieve their structural stabilization.

The SS electrode was immersed in HCl for 10 min and rinsed with deionized water. Acetone was used to further clean the substrates. TiO_2 thin films were produced using pulsed electrophoretic deposition [15–21]. A platinum electrode was used as the counter electrode. The working electrode and the counter electrode were mounted at a distance of 20 mm from each other, perpendicular to the liquid surface in the glass beaker at ambient temperature.

Pulsed electrophoretic deposition was performed using the setup illustrated in Fig. S1. The electrodes were connected to a home-made generator (HP 3314 A) employed in order to produce an AC signal and a digital oscilloscope (Tektronix) used to control the pulsed voltage. The frequency of the pulse cycle was fixed to 10 kHz. It remained steady for each immersion. The pulse time intervals were measured by a field-effect transistor (FET).

The operating parameters were chosen according to references [15, 20, 38]. Thus, the deposition was conducted up to 10 min at a voltage of 20 V and with a duty cycle of 50%. These mixtures between the employed electrophoretic bath and the circuit were qualified to control the definite speed and height of each pulse through the whole deposition process. To obtain a homogeneous and smooth deposition, it is essential that the particles stay totally dispersed and firm. Large particles always have a tendency to deposit due to gravity. To avoid this deposition, the mobility of particles resulting from the application of an electrical field of the pulsed EPD must be higher than that caused by gravity. Therefore, it is challenging to get uniform deposition from the sedimentation of suspension with large particles. Consequently, particles with low weight will have high mobility, which leads to nano-film deposition.

After deposition, the thin films were dried in air for 1 day. To test the effect of heat treatment on crystallinity and related photocatalytic activity in a later stage [35], two working electrodes (one over SS and the other over a CL) were dried in a box-type furnace. The calcination temperature was 550 °C for 4 h 30 min with a heating rate of 2.5 °C/min [20].

Characterization of the films

Microtrac s3500 was used to examine the size distribution of the synthesized particles. It used three precisely placed red laser diodes to characterize particles. The S3500 measures particle size ranging from 0.02 to 2800 microns.

The crystalline structures of thin films were examined by X-ray diffractometer (DRX model X'Pert Pro, PANalytical) by means of Cu $K\alpha$ ($\lambda = 1.5405980$). The presence and ratio of the different crystalline phases in the film were verified by XRD [39].

SEM–EDAX spectra of nano-TiO_2 were carried out with a LaB_6 Scanning Electron Microscope (JEOL JSM-5400LV) operating at 0–30 kV. The coatings were protected before observations with a conductive carbon layer to prevent any charging effects.

Nano-indentation was performed by the Nano-indenter NHT^2 (CSM Instruments, Switzerland) using a Berkovich three-sided pyramidal diamond indenter with a nominal angle of 65.3° and a nominal radius curvature of 20 nm at a normal load of 100 mN and a sliding velocity of 1 $\mu m\ min^{-1}$. The measurements were taken with the load control mode. Load–displacement curves were attained employing the Oliver and Pharr method [40]. From the load–penetration curves, surface hardness (H) and Young's modulus (E) were determined.

Scratch test was realized at ambient temperature via the same apparatus using a Rockwell spherical diamond tip with a radius of 50 μm. The tests were achieved by increasing the load from 30 mN to 15 N (load rate 30 N/min) with a table speed of 6 $mm\ min^{-1}$ over a distance equal to 3 mm.

Adhesion strength of the coating, confirmed by the optical observations of the scratch track, was determined from the loads, at which cracking and delamination occurred, and from the variation of friction force.

The hydrophilic property was calculated by examining the water contact angle of TiO_2 thin films using a contact angle meter (ATTENTION, THETA).

The photoluminescence (PL) was measured at room temperature employing a PerkinElmer LS 55 fluorescence spectrophotometer. The excitation wavelength was 270 nm. The analysis of the spectrum was achieved with Gaussian function fitting in Origin 8.5. UV–visible diffuse reflectance spectra were realized using PerkinElmer Lambda 950 spectrophotometer over the wavelength range of 375–600 nm.

Photocatalytic performance

The photocatalytic activity was evaluated using a typical textile dye amido black 10B ($C_{22}H_{14}N_6Na_2O_9S_2$, $M = 616.5$). The decolourization of amido black (AB) in aqueous solution was monitored at ambient temperature. In each experiment, the coated electrode was immersed into quartz vessel containing 100 ml of amido black 10B (AB-10B) solution with a concentration of 10 mg/l. Before the irradiation, the electrode was immersed in the dark for 30 min to achieve the adsorption equilibrium of AB onto the catalysts. Then, we stirred the solution exposed to UV light. A high-pressure mercury lamp (HPK 125 W, Cathodeon) was applied as a UV excitation source ($\lambda = 365.5$ nm). A noticeable peak at 617 nm and two small peaks at 226 and 318 nm characterized the absorbance spectra of AB-10B. The concentration of the AB was monitored using a UV–Vis spectrophotometer by examining the main absorbance at 617 nm. Chemical oxygen demand (COD) analysis was performed as mineralization test. The COD elimination was calculated employing the following formula [41]:

$$\text{COD elimination } \% = \left(\frac{\text{COD}_0 - \text{COD}_t}{\text{COD}_0}\right) \times 100, \qquad (1)$$

where COD_0 and COD_t indicate the COD before and after decolourization, respectively.

Results and discussion

Structural characterization of titania catalysts films

Figure 2A represents the XRD patterns of the SS substrate before and after the conversion bath.

The two peaks at $2\Theta = 43.61°$ (hematite) and $2\Theta = 50.78°$ (magnetite) refer to the substrate made of SS 316L (Fig. 2A-ii). After immerging our substrate into the conversion bath, there appeared other peaks of hematite (Fe_2O_3) structure at $2\Theta = 24.12°$ (012) and 33.2° (104) as well as an increase in the $2\Theta = 43.47°$ (202) peak intensity. As a result of the aggressive nature of the conversion bath, there was direct chemical attack of metal surfaces to produce oxide metal. The sample showed the presence of magnetite (Fe_3O_4) at $2\Theta = 35.6°$ (311) and 50.7° (003).

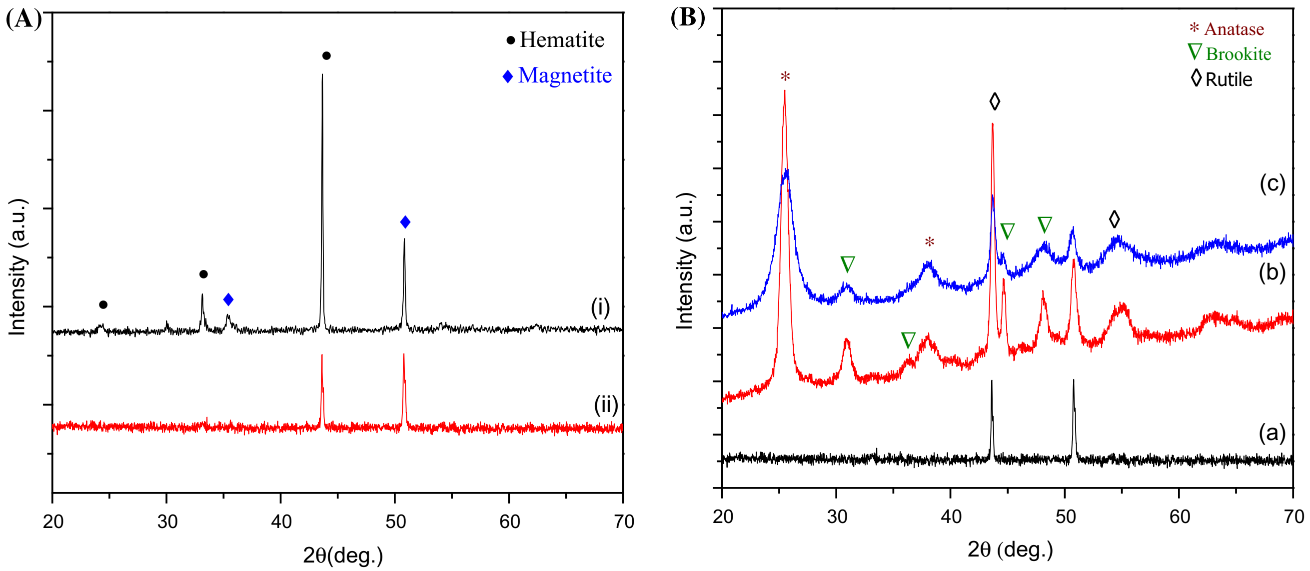

Figure 2 **A** XRD patterns of (*i*) conversion layer and (*ii*) bare stainless steel; **B** XRD patterns of different thin films: (*a*) bare SS, (*b*) annealed TiO_2/SS, (*c*) non-annealed TiO_2/SS.

For quantitative phase analyses, the preferential orientation of the CL films was studied by calculating the texture coefficient [TC (hkl)] using the following formula [42, 43]:

$$TC_{(hkl)} = \frac{I_{(hkl)}/I_0}{(1/N)\sum I_{(hkl)}/I_0}, \qquad (2)$$

where TC (hkl) is the texture coefficient of the plane specified by Miller indices (hkl), I represents the measured intensity, I_0 corresponds to the standard intensity, and N refers to the number of planes observed in the X-ray diffraction pattern.

The deviation of the texture coefficient from unity implied the preferred orientation of the growth of the thin film. TC values of CLs are given in Table 1 showing that the film is highly oriented along (202) plane due to the high crystallinity of hematite.

Figure 2B-b-c shows the intensities of diffraction peaks of TiO_2 over SS with and without calcination. The reflections at the angles $2\Theta = 25.3°$ (101) and 37.98° (004) confirm the presence of anatase phase. The peaks at 30.8° (121), 36.2° (012), 44.6° (114), and 48.12° (231) reveal the existence of brookite, whereas that at 54.1° (211) corresponds to rutile phase. The percentages of the different crystalline phases are represented in Table S1. The crystallite size was approximated using the full width at half maximum (FWHM) of the intense diffraction peaks of crystal phase according to the Scherrer formula [44]:

$$D = \frac{K}{\beta \cos \theta}, \qquad (3)$$

where D is the mean size of the crystalline; K stands for a dimensionless shape factor of about 0.9; λ corresponds to the X-ray wavelength; β represents the line broadening at half the maximum intensity (FWHM) in radians; and θ refers to the Bragg angle (in °).

Table 1 Different texture coefficient [TC (hkl)] values of the CL

	$TC_{(012)}$	$TC_{(104)}$	$TC_{(311)}$	$TC_{(202)}$	$TC_{(003)}$
Pos. [°2Th.]	24.12°	33.2°	35.6°	43.47°	50.78°
CL					
Hematite	0.100	0.496	–	3.118	–
Magnetite	–	–	0.045	–	1.040

Figure 3 represents the XRD patterns of TiO_2 film over the CL before and after annealing the thin film. The peaks of the non-annealed film over CL (Fig. 3c) are the same as those of the non-annealed film over bare SS (Fig. 2c). The absence of the peaks corresponding to the substrate in both cases refers to the presence of TiO_2 thick film. Nevertheless, the annealed film (Fig. 3b) has peaks linked to the CL (Fig. 2A-i) at $2\Theta = 24.12°$, 33.2°, and 35.6°.

The hematite (diameter of 16.8 nm) appeared at the surface of the SS substrate after the treatment in a

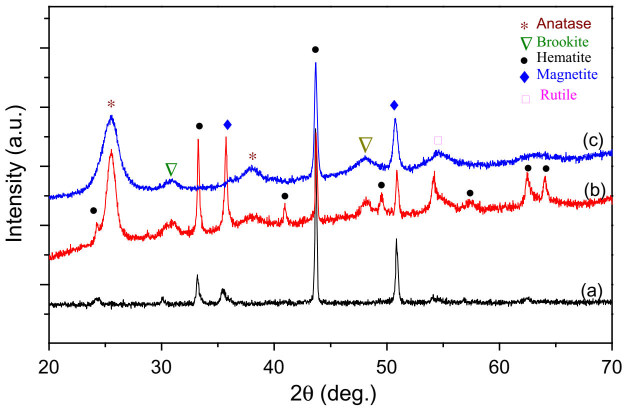

Figure 3 X-ray diffraction patterns of different thin films: (*a*) conversion layer; (*b*) annealed TiO_2 deposited over CL; (*c*) non-annealed TiO_2 deposited over CL.

conversion bath. Once TiO_2 was deposited over the CL and the new film was calcined, the hematite structure was observed again (Fig. 2b) with a diameter of 83.14 nm. This could be explained by the presence of cracks and the output of Fe_2O_3 to the surface under temperature effect.

Table S1 shows the crystallite size of the different phases calculated by the Scherrer formula as mentioned before. (Anatase diameter is D_A, rutile diameter is D_R and brookite diameter is D_B.) The mass fractions of anatase W_A, rutile W_R, and brookite W_B were calculated as shown in Eqs. (4), (5), and (6). K_A and K_B are coefficients with values equal to 0.886 and 2.271, correspondingly as in Ref. [39].

$$W_A = \frac{K_A A_A}{K_A A_A + A_R + K_B A_B}; \tag{4}$$

$$W_R = \frac{K_R}{K_A A_A + A_R + K_B A_B}; \tag{5}$$

$$W_B = \frac{K_B A_B}{K_A A_A + A_R + K_B A_B}, \tag{6}$$

where anatase intensity is A_A, rutile intensity is A_R, and brookite intensity is A_B.

The anatase crystallites become bigger in size with a subsequent decrease in the mass fraction of their grain under the influence of the annealing temperature. Brookite is the most metastable phase, and its crystal size was generally between 11 and 35 nm. Therefore, it would convert straight to rutile. However, anatase may be transformed to rutile or brookite and then to rutile. Anatase to rutile phase transformation is claimed to rise either at the grain edge [45] or inside the grains [46, 47]. The rutile nuclei form and rise in size by consuming the surrounding anatase. If the rutile nuclei form inside the anatase crystallites, the rutile grain growth goes exponentially with temperature. However, in our case, there was shrinkage in the rutile crystallite size, which can be explained by the formation of rutile nuclei on the surface of anatase particles [46]. The volume fraction of the two phases approved the intensity of their XRD peaks.

A typical micrograph of the CL revealing the attacked surface containing many cracks is presented

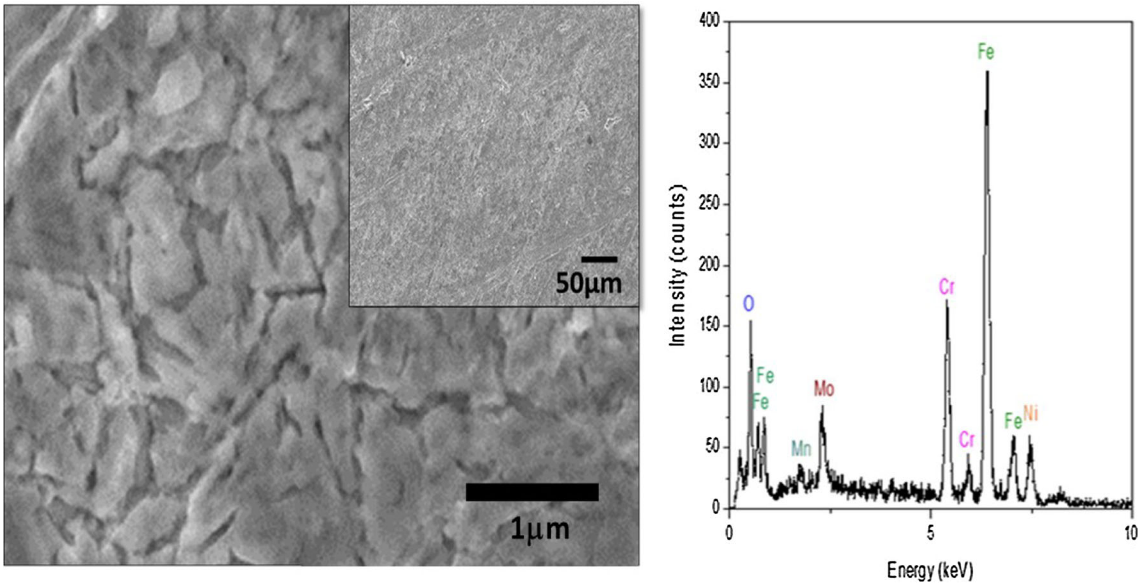

Figure 4 SEM micrograph and EDAX spectrum of the conversion layer.

in Fig. 4. This cracked morphology is similar to the morphology of treated substrates in a conversion bath, as reported in the literature [34].

Once the SS substrates were immersed in the conversion bath, they were attacked by the aggressive medium, which created cracks in the substrate. Moreover, the energy-dispersive X-ray (EDAX) spectrum depicted in Fig. 4 indicates that the obtained product is mainly composed of Fe_2O_3 as shown before by XRD analysis. The innumerable peaks are related to additional elements composing the SS, namely Cr, Ni, Mn, and Mo.

From the scanning electron microscopic images (Fig. 5), it is clear that TiO_2 thin films were made, before calcination, of smaller aggregated particles, resulting in a high porous volume due to aggregation between tiny TiO_2 particles. Equally, after heat treatment, the films were composed of bigger agglomerated particles which may result from the phase transformation from anatase to rutile (as shown in Table S1). In addition, it could be attributed to smaller particles interaction that causes their aggregation into particles with bigger sizes.

The average sizes of the primary particles predictable from the SEM images are presented earlier in Table S1. These sizes are in good arrangement with those calculated from the XRD pattern using the Scherrer equation. Additional reflection shows that the large number of mesopores is caused by the aggregation of primary particles or crystallites.

The surface revealed different grain sizes with the presence of some cracks, especially in the case of annealed TiO_2 over SS (Fig. 5c). These cracks could be explained by the quick evaporation of water during annealing, thickness of TiO_2 film, and the large variance of coefficient of thermal expansion between the substrate and TiO_2 thin film.

EDAX spectra of TiO_2 over SS showed well-definite peaks corresponding to Ti along with a peak of oxygen, while the other metals in the alloy did not appear.

After heat treatment, Fe and Cr appeared. These elements descended from the passive film on top of the pitted zone (cracks) caused by calcination. Fe was derived from iron oxide as presented before in XRD analysis (Fig. 2).

Nonetheless, Cr appearance resulting only from calcination was due to its small trace as initial material in the substrate surface. Table S2 shows the composition of both ordinary SS 316L and CL. In our study, we obtained a mixture of new austenitic stainless steel by reducing the nickel content and increasing both molybdenum and manganese. Some metal species impurities can act as recombination centers for charge carriers during photocatalysis [48–51]. However, in case of TiO_2 over a CL, EDAX spectra showed the presence of Ti, O, and Fe elements. After annealing the TiO_2/CL film, there appeared some trace of C.

Thickness of the films

To investigate the thickness of the different deposited TiO_2 layers, two methods were used.

The first technique is a theoretical thickness measurement which consists in calculating the depth of the electrons penetration using the Castaing formula [52] given by:

$$R(\mu m) = 0.033E_0^{1.7}\ (A/\rho Z),$$

where ρ represents the volume density (g cm^{-3}), E_0 is the energy of the electrons, A corresponds to the atomic mass, and Z denotes the atomic number of the film.

Experimentally, the primary energy (E_0) of the electrons was gradually increased by detecting the characteristic peaks of the coating by EDAX. At the appearance of the characteristic peaks of the substrate, we noted the value of E_0 used to determine the range R corresponding to the coating thickness. Figure S2 shows the evolution of the range as a function of the primary energy in the case of titanium dioxide ($A = 25.99$, $Z = 12.40$, $\rho = 2.39$).

The second method is cross-observations by SEM allowing the measurement of film thickness (Fig. 6). Table 2 presents the thickness of all TiO_2 films obtained by applying the two previously mentioned techniques. The theoretical thickness measurements are in good agreement with the SEM measurements. Correspondingly, the feeble difference between theoretical and experimental values is in the range of error bar.

With annealing temperature, there is an observed increase in the films thickness for both TiO_2/CL and TiO_2/SS, which demonstrates that calcination considerably affects the thickness of the deposited film [53–55]. The film thickness growth was attributable to the increase in the grain sizes with the annealing temperature. At high temperatures, atoms had sufficient diffusion activation energy to inhabit the site in

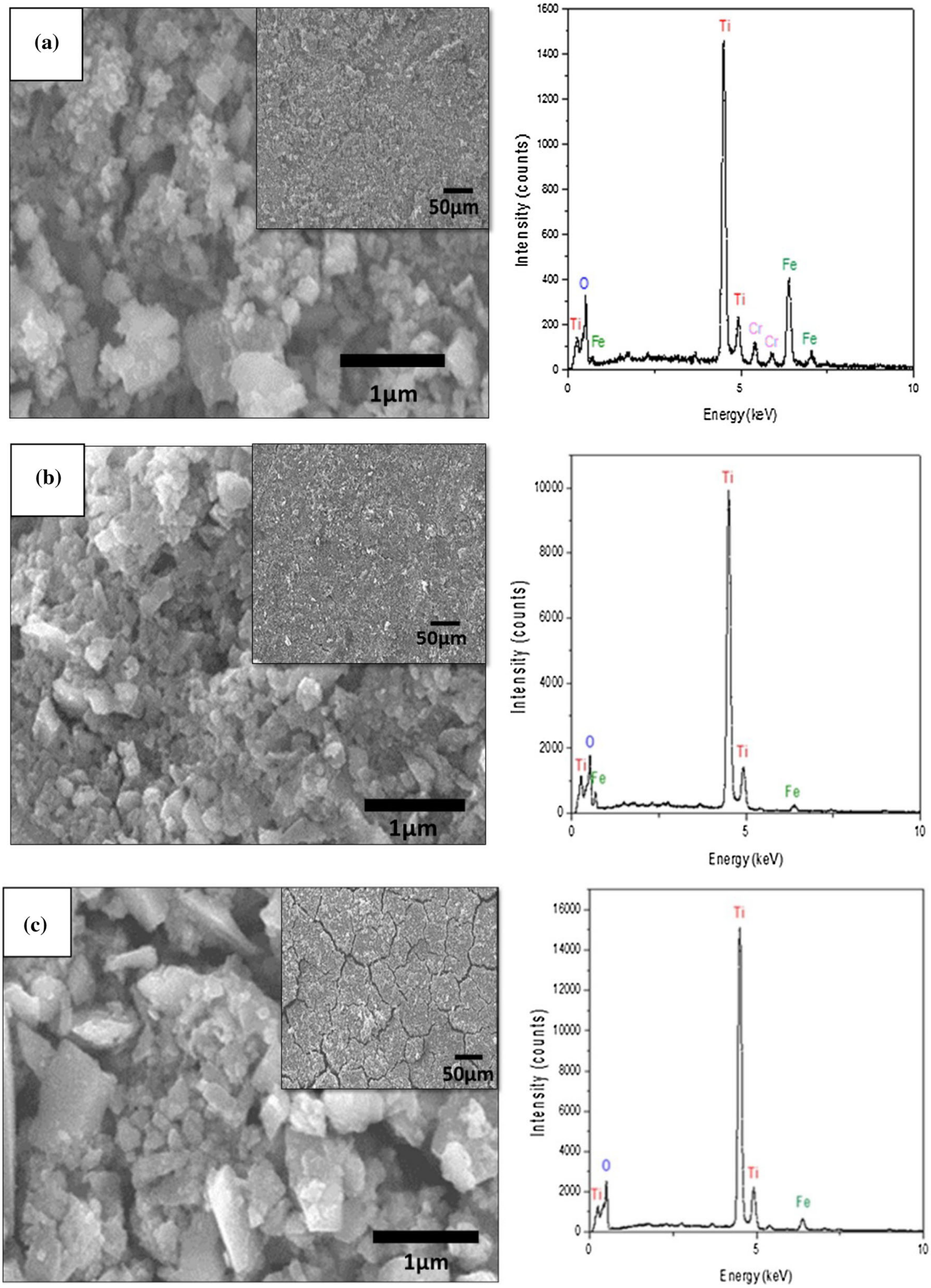

Figure 5 SEM images and EDAX of: **a** annealed TiO_2 over a CL; **b** non-annealed TiO_2 over a CL; **c** annealed TiO_2 over SS; and **d** non-annealed TiO_2 over SS.

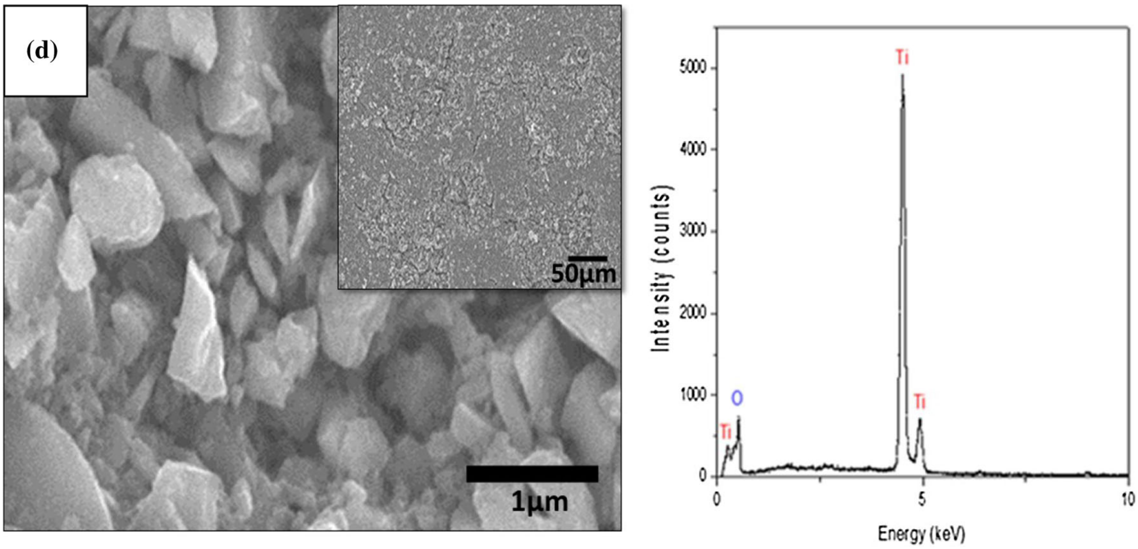

Figure 5 continued.

crystal lattice and the grains with inferior surface energy become larger [56]. This result is in agreement with XRD data shown in Table S1.

Studies in [57–59] revealed that TiO_2 film thickness affects its optical performance as it is demonstrated in Fig. 10.

Mechanical properties

The mechanical strength of the coatings is a vital condition for industrial applications. Figure 7 illustrates the evolution of the normal force as a function of penetration depth obtained by nano-indentation for the TiO_2 coating. First, it is worth noting that all curves exhibit a similar plastic deformation. The observed imprint was permanent and did not show an elastic relaxation. Table 3 depicts the hardness and the elasticity modulus of TiO_2 thin films deposited over bare SS and CL, annealed (Fig. 7a–d) and non-annealed (Fig. 7b–c). The annealing temperature and the presence of a CL remarkably influenced the mechanical properties of the deposited film. The smooth and crack-free morphology of the TiO_2/CL coatings led to a stable and adhesive coating to the substrate, which was attributed to the intermediate layer (CL) linking the TiO_2 nanoparticles and the SS. Nevertheless, in the case of the coating prepared without CL and due to the important cracks and augmented surface roughness, the TiO_2 film could be detached easily.

There was an increase in the values of both the elasticity modulus and the hardness of the TiO_2 thin films deposited over a CL compared to those on SS [16]. These results suggested an improvement of the coating adhesion. Moreover, annealing the films reduced the Young's modulus, which badly affected the adherence of the film [30].

In fact, no considerable difference in E and H between all deposited films was observed. Besides, the annealed films had a slightly greater Young's modulus and hardness. Generally, the microstructure of the thin film plays a serious role in defining its mechanical responses [60]. Increasing temperature creates structural modifications behind the variations in hardness levels. The rise of the film hardness, in our case, could be explained by the growth of the structure into a more compact one compared to the structure obtained before heat treatment [61]. It should be highlighted that porosity is of ultimate significance on material properties. The primary synthesis methods often lead to porosity and incomplete bonding among the grains. Processing imperfections, as porosity, may damage the properties of nano-crystalline materials as it was proved in other works [62]. Weertman et al. [63] showed the Young's modulus decrease as a function of porosity for nano-crystalline Pd and Cu. The decrease in Young's modulus with porosity has been recognized and definitely spoken in many mechanics simulations.

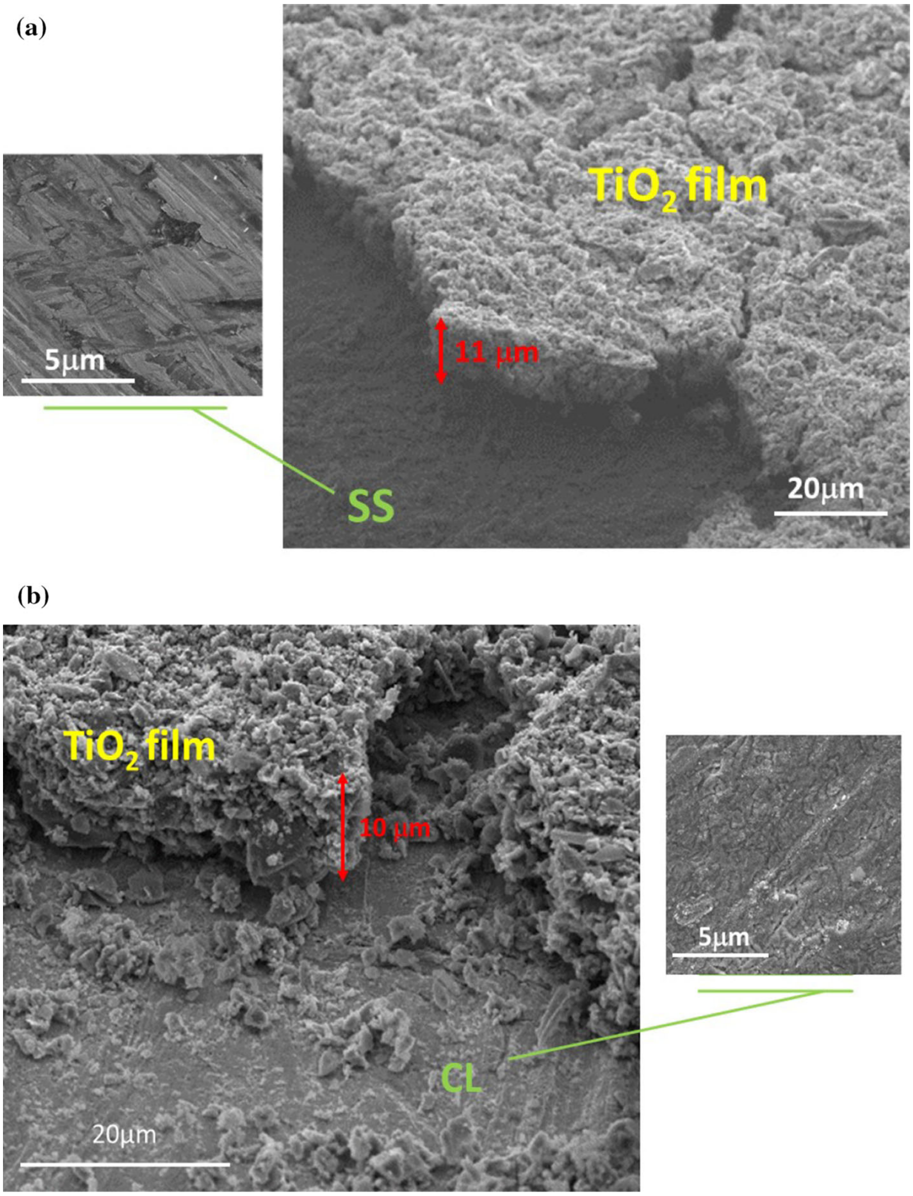

Figure 6 SEM cross-sectional images of **a** non-annealed TiO_2/SS and **b** annealed TiO_2/CL.

Table 2 Thickness values of TiO_2 films

	As-deposited films		Annealed films	
	TiO_2/CL	TiO_2/SS	TiO_2/CL	TiO_2/SS
Experimental measurement (µm)	8.5 ± 1.2	11 ± 1.1	10 ± 1.3	25 ± 1.5
Theoretical measurement (µm)	8.84 ± 0.2	11.59 ± 0.3	10.45 ± 0.4	25.44 ± 0.9

The decrease in E, in our work, could be attributed to the modification of the microstructure properties from a compact and dense morphology without cracks into a structure having a lot of cracks and voids. As shown in the SEM images, with the annealing of the deposited film, the number of cracks increased.

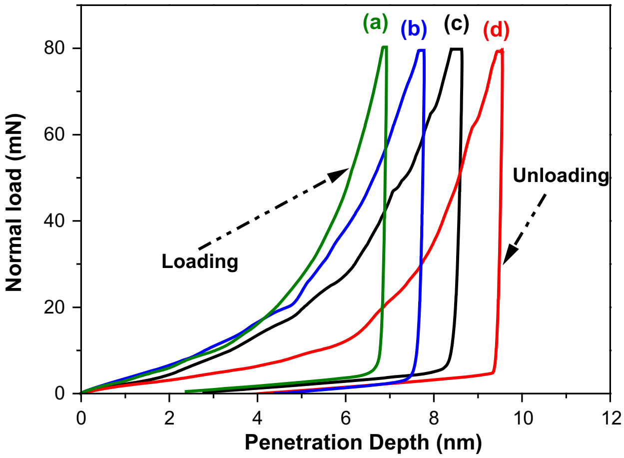

Figure 7 Nano-indentation curves carried out on the TiO_2 coating over: (*a*) SS with annealing, (*b*) SS without annealing, (*c*) CL without annealing, and (*d*) CL with annealing.

Adhesion properties

The scratch test was carried out for the characterization of adhesion. It involves three distinct stages: the measurement of the initial profile of the surface to scratch, called "pre-scratch," the scratch step, and finally the measurement of the final profile in scratch background "post-scratch." The presence of brute spallation, a large area isolated even using the lower load in the machine, is a sign of low adhesion strength.

The different adherence failures can be identified by: L_{C1}, the lower critical load, defined as the load at which the first cracks occurred (cohesive failure); L_{C2}, the upper critical load at which the first delaminating at the edge of the scratch track happened (adhesion failure) [64]; and L_{C3}, the load obtained when the damage of the film exceeded 50% [65]. Figure 8 presents the result of scratch test performed on a non-annealed TiO_2 coating over CL.

We got good adhesion since the spallation of the coating was slow as the applied force increased. Thin films with CL showed enhanced adhesion compared to those over a SS. Table 4 represents the theoretical load values of the different films obtained from the friction–load curves.

In this work, we propose, for the first time, the use of a CL to improve the adhesion of the TiO_2 film over the SS substrate. Comparing our results to those obtained in [16, 17] proves that the presence of a CL over a SS substrate increases the adhesion of TiO_2 film. Indeed, L_{C1} in case of TiO_2/CL (L_{C1} = 1.8–8.2 N) film is higher than L_{C1} in case of TiO_2/SS as shown in references [16] (L_{C1} = 969.473–1177.968 mN) and [17] (L_{C1} = 53.78–345.74 mN).

In addition, the increase in the critical load associated with adhesive limit demonstrates that the annealing treatment improves the coating adhesion to the substrate. This improvement was due to the enhancement of the mechanical anchorage inside the substrate roughness. The chemical affinity between the TiO_2 coating and the substrate as well as the existence of cracks and other flaws affected the mechanical properties of TiO_2 coating and the adhesion of the deposited films.

Thin film wettability

Table 5 shows the result of contact angle measurements for water on the TiO_2 coating films deposited over bare SS and a CL. For both cases, the contact angles for water on the TiO_2 coating films decreased by annealing the thin film.

In case of non-annealed films, TiO_2/CL presented lower contact angle than TiO_2/SS. Besides, the functionalized surface with a CL did not contain hydroxyl and water could not come into the interior region of the coating films. The annealed TiO_2 films had large particle sizes as shown by XRD analysis (12.65 nm for TiO_2/SS and 9.74 nm for TiO_2/CL) and in SEM pictures (Fig. 4a, c), which induces a progress of the roughness and the water contact surface. These important modifications were caused by conversions

Table 3 Young's modulus and hardness of the different TiO_2 films

	Hardness (*H*) [MPa]	Elasticity modulus (*E*) [GPa]
TiO_2/SS		
Without annealing	42.194 ± 0.32	8.429 ± 0.15
Annealed at 550 °C	51.015 ± 0.44	7.140 ± 0.11
TiO_2/CL		
Without annealing	50.573 ± 0.42	16.844 ± 0.23
Annealed at 550 °C	63.850 ± 0.67	12.470 ± 0.19

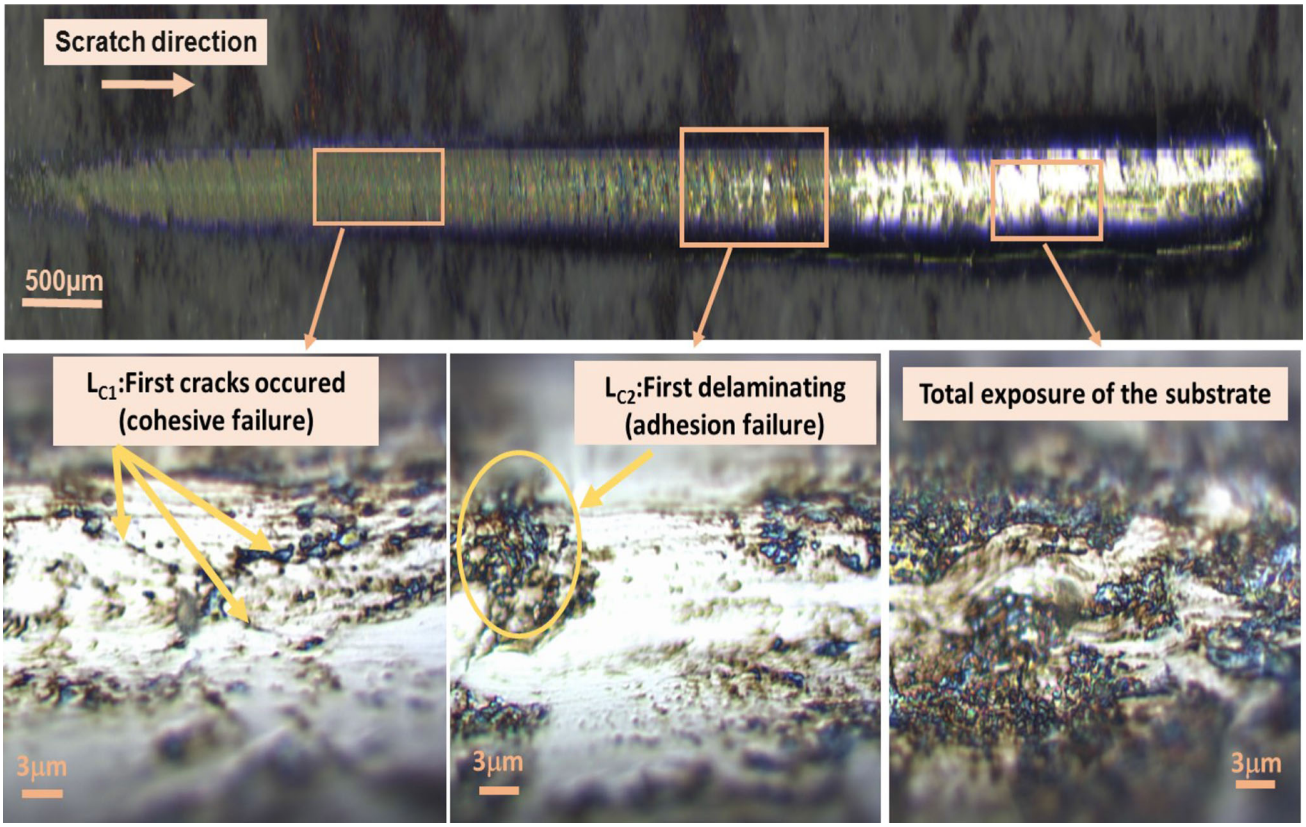

Figure 8 Scratch test of as-deposited TiO_2/CL coating.

Table 4 Critical loads of TiO_2 thin films

	Without annealing		After annealing at 550 °C	
	L_{C1} (N)	L_{C2} (N)	L_{C1}(N)	L_{C2}(N)
TiO_2 over SS	1.5 ± 0.12	6.9 ± 1.5	7.1 ± 1.6	10.5 ± 2.5
TiO_2 over CL	1.8 ± 0.15	7.5 ± 1.8	8.2 ± 2.1	12 ± 2.8

Table 5 Contact angle measurements of the different deposited films

	Annealed TiO_2/SS	Annealed TiO_2/CL	Non-annealed TiO_2/SS	Non-annealed TiO_2/CL	CL	Bare SS
Contact angle measurement	5.15° ± 1.5	6.55° ± 2.1	29.79° ± 9.5	19.39° ± 7.3	99.29° ± 21	109.60° ± 25

in the surface morphology and/or chemical condition of the film surface. Therefore, the contact angles for water after annealing were low. The increase in the adsorbed hydroxyl groups on the surface would upswing van der Waals forces and hydrogen bond interactions between water molecules and hydroxyl group [66]. Then, water could completely blow out across the surface and the hydrophilicity could be retained for long time.

It should be noted that, for both annealed films, photocatalytic activities could decrease due to their larger particles size and superhydrophilicity [67–69]. For the conversion layer, a large contact angle corresponding to hydrophobic surface ($\theta \geq 90$) was obtained. The water tended to form droplets over the surface of the coating. Then, it spread completely. Even slight variations in surface roughness can lead to improved wetting properties.

Optical properties

Photoluminescence (PL) spectroscopy is a nondestructive method employed to examine the electronic structure of materials. PL spectra demonstrate the existence of lattice defects, recombination of the photogenerated electron–hole pairs, self-trapped excitons, immigration, and oxygen vacancies [70, 71]. The photoluminescence spectra of the different deposited thin films are presented in Fig. 9A. From the deconvolution and peak fitting, we notice an intensive photoluminescence at a wavelength of around 415 nm and 418 nm corresponding to bare SS and the CL, respectively. This resulted from the oxygen vacancies in Cr or Fe oxides at the surface [72]. Both peaks coexist after the deposition of TiO_2 film, which was due to the strong background obtained from SS and the conversion coating [73, 74]. Moreover, the intensities were remarkably reduced after TiO_2 deposition, which was attributed to the lower PL property of TiO_2. The comparison between the films over SS (Fig. 9B-c-d) and over the CL (Fig. 9B-e-f) indicates that the PL intensity declines by introducing the CL to adjust the optical properties of the substrates.

The PL intensity reduction was caused by charge separation property of TiO_2 films. In general, the higher decrease in the intensity of photoluminescence is due to the lower charge carrier recombination in TiO_2 film [72]. As shown in Fig. 9A, lower intensity was obtained by non-annealed TiO_2/CL followed by the annealed one. From the deconvolution and the peak fitting of the PL intensity (Fig. 9B-c-d-e-f), we notice the presence of the same first band around 397 nm in all curves, which was accredited to the band-to-band transition of TiO_2 [75].

The peak at 442 nm corresponds to the interaction of trapped electrons on Ti 3d orbital with holes existing in O 2p orbital of TiO_2, which generated self-trapped excitons (STE) [76]. However, the emission band at 463 nm was related to the charge transfer transition from Ti^{3+} to oxygen anion in a TiO_6^{8-} complex associated with surface oxygen vacancies [70, 77, 78]. Finally, the low bands at 419 nm and 525 nm could be attributed to the oxygen vacancies [76]. The section of electrical measurements confirms the PL results.

Figure 10 illustrates the UV–Vis diffuse reflectance spectra (DRS) of the different TiO_2 films over SS and CL. The band gap transition as distinguished above in the PL analysis was confirmed in all TiO_2 thin films showing the classic absorption of anatase in the UV region $\lambda < 400$ nm.

The differential diffused reflectance spectra were used to determine all TiO_2 films optical transition energies. The E_g values were 3.49 eV for annealed TiO_2/CL, 3.48 eV for non-annealed TiO_2/CL, 3.52 eV for annealed TiO_2/SS, and 3.50 eV for non-annealed TiO_2/SS (inset of Fig. 10). The non-annealed TiO_2/CL showed lower E_g value. The crystal structure of the TiO_2-deposited film affected its band gap value. From the above-mentioned results, we may conclude that, the thinner the band gap is, the wider the spectral range response and the more efficient the photocatalytic activity are. Obviously, the semiconductor could increase poorer photon energy and produce photoelectrons and holes [79].

Photocatalytic decolourization of amido black (AB-10B)

The photocatalytic properties of TiO_2 thin films under UV light irradiation were investigated using AB-10B as the model contaminant. The photocatalytic efficiency of the coated TiO_2/SS before and after functionalization of the substrate was tested against the decolourization of AB in aqueous solution at natural pH. The decolourization during experimentation is presented in Fig. 11. The CL alone showed a limited photocatalytic efficiency of 13.63%.

According to the obtained curves in Fig. 11, the relationship of (Abs/Abs_0) with respect to irradiation time suggested the first-order model. The effectiveness of dye decolourization for each TiO_2 photocatalyst over SS or CL and after 300 min of illumination is presented in Table 6.

It appeared that the most active one is non-annealed TiO_2/CL. The degree of AB-10B decolourization, in this case, was 63.53% corresponding to an increase in photocatalytic efficiency in the presence of CL. The existence of the hematite from the CL affected significantly the percentage of the decolourization. Therefore, for the annealed film, the photocatalytic activity decreased. This behavior can be attributed mainly to the growth of the crystalline

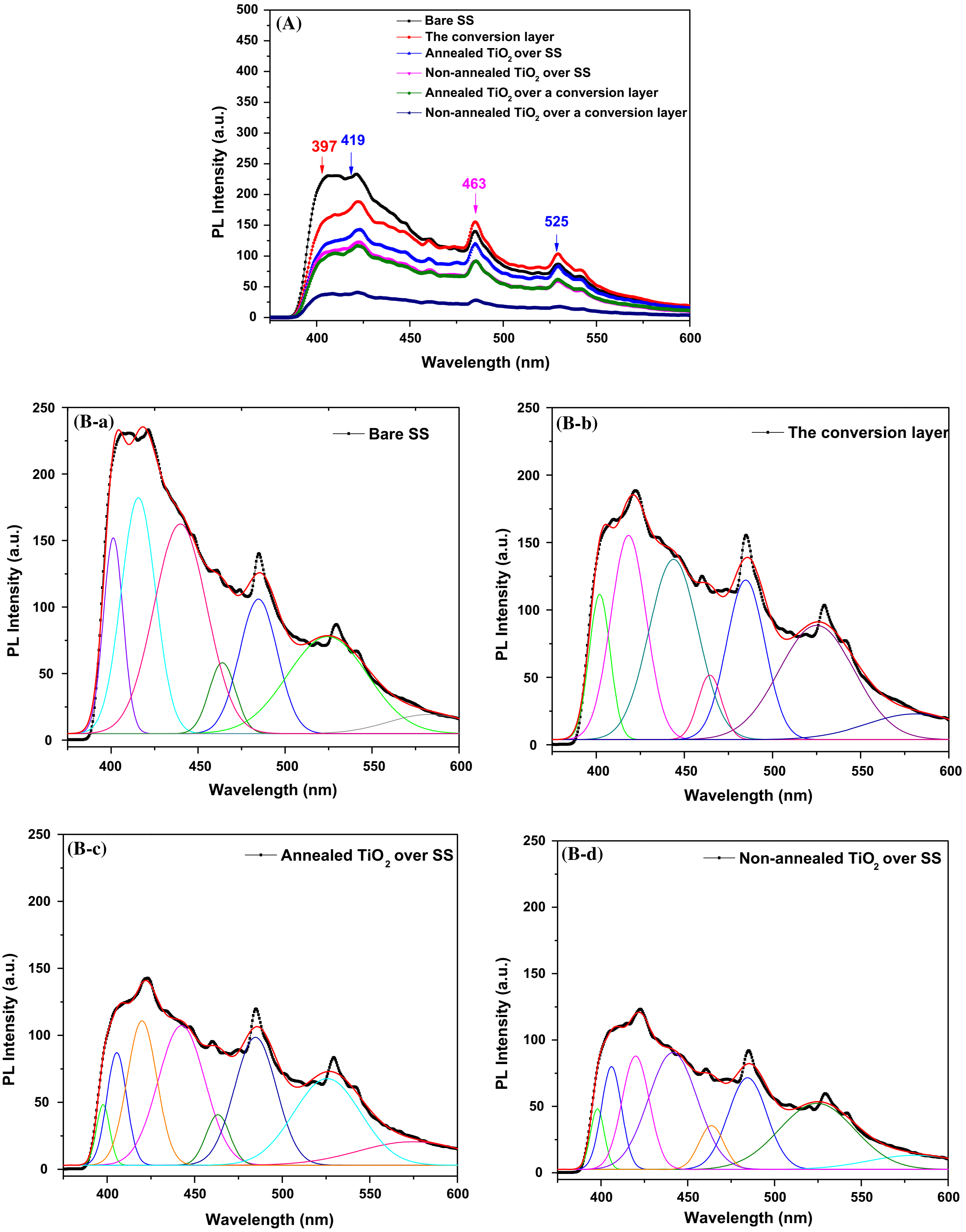
(A)
Bare SS
The conversion layer
Annealed TiO2 over SS
Non-annealed TiO2 over SS
Annealed TiO2 over a conversion layer
Non-annealed TiO2 over a conversion layer
397
419
463
525
PL Intensity (a.u.)
Wavelength (nm)
500
450
400
350
300
250
200
150
100
50
0
400
450
500
550
600
(B-a)
Bare SS
(B-b)
The conversion layer
(B-c)
Annealed TiO2 over SS
(B-d)
Non-annealed TiO2 over SS
PL Intensity (a.u.)
Wavelength (nm)
250
200
150
100
50
0

◀**Figure 9** **A** Photoluminescence spectra of the different thin films excited at 270 nm. **B-a**, **B-b**, **B-c**, **B-d**, **B-e,** and **B-f** deconvolution and peak fitting of PL emission peaks for all studied samples.

size upon annealing. In fact, decreasing the specific area and the transformation of anatase to rutile (Table S1) produced less photocatalytic activity. This finding was confirmed by several authors [36, 80].

Generally, photocatalysis efficiency is a complex process depending on all the presented physical parameters (crystalline form, crystal size, electron–hole recombination, hydrophobic aspect, etc.). In photocatalytic applications, the anatase phase is more efficient than rutile because of its more open structure. The apparent kinetic constant presented a linear dependency with the band gap energy E_g of studied electrodes (Fig. S3a). In addition, decoloration efficiency increased as the anatase percentage rose (Fig. S3b). With increasing W_A, the integrated intensity fell down. The change in the structure of the films affects the PL intensity. The impurity levels can augment the electron–hole pair separation rate in TiO_2 films. They are generated with oxygen vacancies and interstitial oxygen defects. As the redox reactions might take place on the surface of oxygen vacancies and interstitial oxygen defects, the oxygen defects can be considered to be the active sites of the TiO_2 photocatalyst [81–83]. As shown in Fig. 9, the PL emission intensity increases with annealing temperature as well as CL absence, suggesting the reduction in the oxygen defects in TiO_2 films. Therefore, the photocatalytic activity of the TiO_2 films could not be improved. Obviously, the abundant surface oxygen vacancies or defects exist in TiO_2 films, which may play a vital role in the photocatalytic activity.

The TiO_2 over a CL had the maximum anatase mass fraction as indicated in Table S3. It also presented the less PL intensity, which can be contributed to its high degradation percentage.

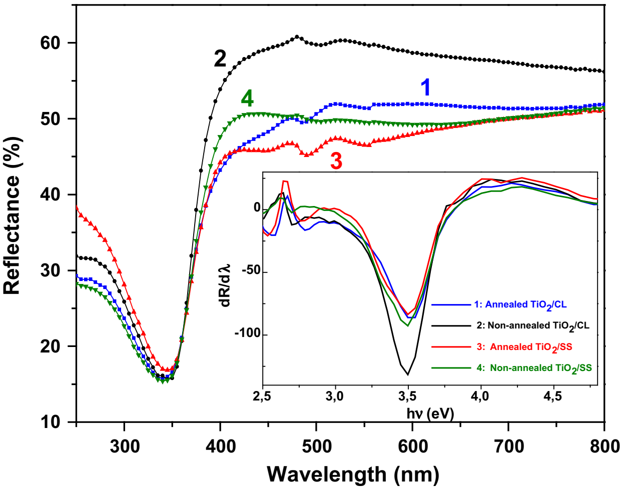

Figure 10 Reflectance spectra for (*1*) annealed TiO_2/CL, (*2*) non-annealed TiO_2/CL, (*3*) annealed TiO_2/SS, and (4) non-annealed TiO_2/SS; inset: first derivative of reflectance (dR) of the different films.

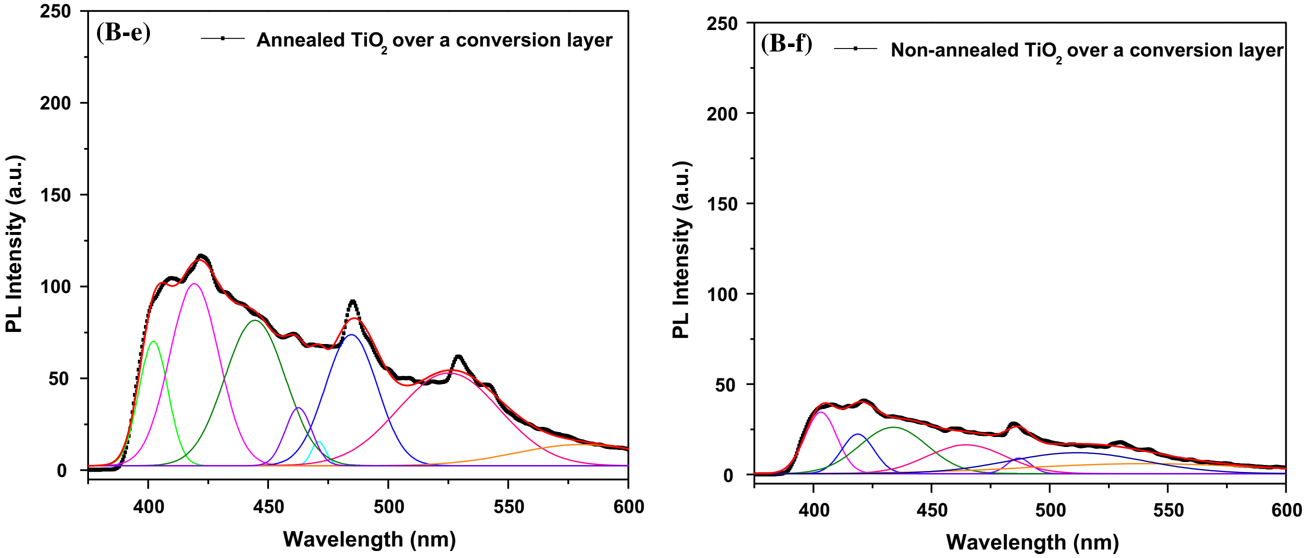

Figure 9 continued.

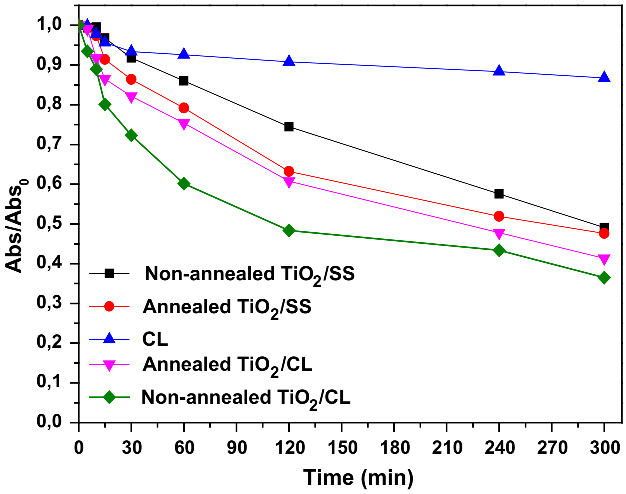

Figure 11 Amido black degradation as a function of time for the different photocatalysts under illumination.

As far as we know, the higher activity of the rutile–anatase mixture of Degussa P25 is due to a typical electron transfer from the conduction band of the anatase to that of rutile [70–73]. Consequently, the anatase–rutile mixed phase blocks the electron–hole recombination by locating electrons and holes in altered crystalline phase. This finding agrees with the results obtained by depositing the mixture of anatase, rutile, and brookite of our synthesized powder over a CL. In our study, the CL (Fe_2O_3) enhanced the photocatalytic activity of TiO_2 coating.

The ternary mixtures of the TiO_2 polymorphic phases were more efficient together with the presence of the hematite form. Hematite Fe_2O_3 was able to absorb photons from the green–blue part of the spectrum between 300 and 600 nm. Its small band gap of 2.1 eV makes it one of the most promising semiconductors for photocatalysis [74]. It was noticed that, among all samples, the non-annealed thin film with an interlayer of Fe_2O_3 showed the best result. Figure S4 reveals a schematic illustration of energy band and photogenerated charge carriers for the TiO_2 and Fe_2O_3, which can explain the good photocatalytic activity of TiO_2/CL and assign it to the creation of TiO_2/Fe_2O_3 heterojunction.

These results were discussed in terms of energy band structure and microstructure [75]. The energy band and the photogenerated charge carriers for the TiO_2 and Fe_2O_3 can explain the improved photocatalytic activity and assign it to the creation of TiO_2/Fe_2O_3 heterojunction [84–86]. As shown in the energy diagram of the interface in Fig. S4, the photoinduced electrons generated in the conduction band (CB) of TiO_2 favored the migration to the Fe_2O_3 phase having a lower CB potential. The electrons will be expended in a reduction process. The elementary field in TiO_2/Fe_2O_3 bilayer and electrons in the valence bands (VB) of TiO_2 were driven into the VB of Fe_2O_3, while photogenerated holes moved into the VB of TiO_2 in an opposite direction [87]. Consequently, these holes would powerfully oxidize a mobile species and the charge transport between VBs of Fe_2O_3 and TiO_2 can be considered as an effective process for stimulating the photocatalytic activity of the TiO_2/Fe_2O_3 thin film electrodes, since this result indicates that the charge recombination was reduced in the process of electron transport. The TiO_2 film over the CL showed crack as illustrated before by SEM images. Therefore, it can create sufficient defect states without blocking the hole transfer.

Furthermore, compared to the annealed hematite/TiO_2 thin film, the small crystal size in the non-annealed one decreased the recombination occurring within the crystals. Besides, it contributed to an additional increase in the photogenerated holes reaching the interface of TiO_2 and the pollutant.

The presence of organic intermediates was in relation to the level of mineralization achieved during the photocatalytic decolourization of AB-10B. Their absence represented a proof of the complete destruction of organic compounds in water, which is of great importance in water treatment. Mineralization level can be evaluated by COD measurement. The COD change during photocatalysis was studied

Table 6 Percentage of decolourization, correlation coefficients (R^2), and rate constant (k min^{-1}) of the apparent first-order kinetic model for photocatalytic degradation of AB-10B over various photocatalysts

	Non-annealed TiO_2/CL	Annealed TiO_2/CL	Non-annealed TiO_2/SS	Annealed TiO_2/SS
% Decolourization	63.53 ± 1.21	58.44 ± 0.95	52.62 ± 0.55	50.63 ± 0.51
Rate constant $k * 10^{-3}$ (min^{-1})	3.18 ± 0.20	2.95 ± 0.18	2.62 ± 0.16	2.47 ± 0.20
Correlation coefficient (R^2)	0.9740 ± 0.005	0.9747 ± 0.006	0.9792 ± 0.004	0.9981 ± 0.005

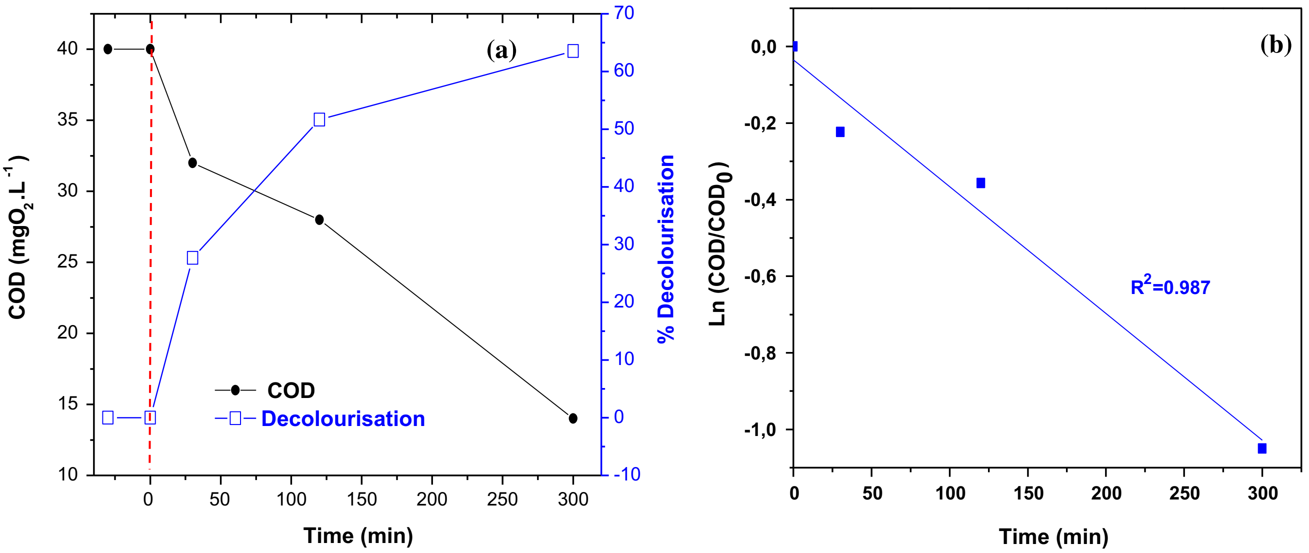

Figure 12 **a** COD evolution during AB-10B photocatalytic decolourization compared to the percentage of decolourization in case of non-annealed TiO_2/CL; **b** kinetics of AB decolourization over non-annealed TiO_2/CL compared to its mineralization.

in the case of the electrode that showed the best photocatalytic activity, which is non-annealed TiO_2/CL as demonstrated in Fig. 12b. The initial concentration was 10 mg/l at natural pH. The COD removal of the dye after 5-h irradiation with UV light is presented in Fig. 12a. Giving to the obtained curve, the relationship of ln(COD/COD$_0$) with respect to irradiation time suggested the first-order kinetic, where the apparent rate constant is found to be $3.31\ 10^{-3}\ \text{min}^{-1}$ with a correlation coefficient of 0.987.

The percentage of COD reduction was 65.00% after 300 min equivalent to 63.53% of dye decolourization. With the extended irradiation time, we could possibly achieve a complete mineralization. After materials characterization, the application of the synthesized TiO_2 films was explored in the photocatalysis degradation of AB-10B. The current samples are compared to other reports on TiO_2 deposited with different and more common techniques. In the literature, a few modern studies [88–93] considered the mechanical properties of TiO_2 layers using nano-indentation method. Nevertheless, in this work, mechanical properties were combined with photocatalytic characteristics. Table 7 presents an extensive literature overview of previous works on TiO_2 properties.

These TiO_2 thin films were deposited, for instance, by sol–gel dip-coating method [88, 89], pulsed laser deposition [90], filtered arc deposition [91], electrochemical deposition [92], sputtering [93], or EPD [16, 17] on a variety of substrates. The existing hardness, Young's modulus data, and photocatalytic properties reported the average data of the different TiO_2 films. Relying on the characteristics of the films and the type of substrates, the values of hardness and Young's modulus values were between 22 MPa and 19 GPa for hardness, and from 7 to 209 GPa for Young's modulus. In our case, the values of hardness and Young's modulus values were more similar to those presented in references [16, 17]. This may indicate that these comparable properties are linked to the deposition method (pulsed EPD) due to its important influence on the films morphologies. The photocatalytic activities were affected also by the variation of the film thickness and the particles size of the TiO_2 film as well as the presence of Fe_2O_3 as mentioned before (heterojunction effect). Consequently, more photocatalytic action can be achieved.

Conclusion

The microstructure of TiO_2 films considerably affected the photocatalytic activity. In order to have an extremely active photocatalytic thin layer, new electrode materials were considered. This study examined the photocatalytic activity of nano-structured

Table 7 Techniques, conditions, and experimentally determined values published in the literature for mechanical and photocatalytic properties of TiO_2 coatings

Layer and deposition mode		Adhesive properties	Mechanical characteristics		Photocatalytic properties	Refs.
Thin film	Process		Hardness H (GPa)	Young's modulus E (GPa)		
TiO_2	Sol–gel dip-coating	–	7.9	176	–	[89]
Rutile TiO_2	Sputtering	–	11–12	160–170	–	[93]
TiO_2	Sol–gel dip-coating	The quality of adhesion according to ISO 2409 standard is excellent	–	–	50% degradation of methylene blue	[88]
TiO_2	Pulsed laser deposition	–	6.69	195.5	–	[90]
TiO_2	Filtered arc deposition	–	11.6–18.5	140–225	–	[91]
TiO_2	Electrolytic deposition	Excellent behavior during scratch tests with no signs of delamination	5.5–6.6	228 GPa on steel and 116 GPa on TiAlV	–	[92]
TiO_2 (P25)	DC electrophoresis	$L_{C1} = 969.473–1177.968$ mN	Between 41.107 and 527.105 MPa	17.231–36.857	87.7% of AB-10B degradation (10 mg L^{-1}) $K = 9.7910^{-5}$ min^{-1}	[16]
P25/PVP	DC electrophoresis	$L_{C1} = 53.78–345.74$ mN	22–140 MPa	7–25	47.83% of AB-10B degradation (10 mg L^{-1})	[17]
TiO_2	Pulsed electrophoretic deposition	$L_{C1} = 1.8–8.2$ N $L_{C2} = 6.9–12$ N	42.194–63.850 MPa	7.140–12.470	63.53% of AB-10B degradation (10 mg L^{-1}) $K = 3.18\ 10^{-3}$ min^{-1}	Our work

TiO_2 thin films to be used in the degradation of organic pollutants. The effect of thermal annealing and the CL on the structural, morphological, and photocatalytic properties of nano-structured TiO_2 thin films was also investigated.

A novel supported photocatalyst on SS was prepared by TiO_2 deposition using pulsed EPD. The used TiO_2 powder was prepared by hydrolysis of $TiCl_4$ followed by dialysis. An interlayer CL composed mainly of Fe_2O_3 was formed on the SS surface with the intention to strongly improve the film adhesion. The electronic interaction between CL and the TiO_2 coating was also marked to decrease electron–hole recombination increasing TiO_2 layer efficiency.

The as-deposited nano-structured TiO_2/CL thin film prepared by pulsed EPD exhibited highly enhanced photocatalytic activity toward UV light-driven photocatalytic degradation of AB dye in water, as compared to the annealed samples. This enhanced photocatalytic activity was attributed to the combined effects of three-phase structure, TiO_2/Fe_2O_3 heterojunctions, and smaller size of TiO_2 nanoparticles providing higher surface area for higher dye adsorption and efficient photocatalytic degradation upon UV irradiation.

The annealing treatment did not bring an improvement in the photocatalytic activity because of the growing size of TiO_2 nanoparticles and the important change in the crystal structure of TiO_2 thin film. The non-annealed TiO_2/CL presented a COD removal of 65.00% and a dye decolourization of 63.53% after 5 h.

The current technique can be considered as a simple approach and low-cost heading for synthesizing an active photocatalyst. The deposited film had advanced mechanical properties and showed no adhesion difficulty. These characteristics are very promising in photocatalytic coatings for practical environmental applications.

Acknowledgements

This research was undertaken under the frame of the Contract Programme between the Center of Water Research and Technologies (CERTE) and the Ministry in charge of the research in Tunisia. It is carried between the Laboratory of Wastewater and Environment of CERTE and the National High School of Engineers of Tunisia.

Electronic supplementary material: The online version of this article (https://doi.org/10.1007/s10853-017-1755-5) contains supplementary material, which is available to authorized users.

References

[1] Zangeneh H, Zinatizadeh AAL, Habibi M, Akia M, Hasnain IM (2015) Photocatalytic oxidation of organic dyes and pollutants in wastewater using different modified titanium dioxides: a comparative review. J Ind Eng Chem 26:1–36

[2] Grätzel M (2001) Review article: photoelectrochemical cells. Nature 414:338–344

[3] Fox MA, Dulay MT (1993) Heterogeneous photocatalysis. Chem Rev 93:341–357

[4] Wang R, Hashimoto K, Fujishima A, Chikuni M, Kojima E, Kitamura A, Shimohigoshi TM (1997) Watanabe light-induced amphiphilic surfaces. Nature 388:431–432

[5] Kamat PV (1993) Photochemistry on nonreactive and reactive (semiconductor) surfaces. Chem Rev 93:267–300

[6] Ismail M, Bousselmi L (2010) Effect of adsorption on the photocatalysis performance of anthraquinone dye. Water Sci Technol 61:2539–2548

[7] Bousselmi L, Geissen SU, Schroeder H (2004) Textile wastewater treatment and reuse by solar catalysis: results from a pilot plant in Tunisia. Water Sci Technol 49:331–337

[8] Wang XT, Wei QY, Zhang L, Sun HF, Li H, Zhang QX (2016) CdTe/TiO_2 nanocomposite material for photogenerated cathodic protection of 304 stainless steel. Mater Sci Eng, B 208:22–28

[9] Zhang L, Wang XT, Liu FG, Sun HF, Li H, Wei QY, Hou BR (2015) Photogenerated cathodic protection of 304ss by ZnSe/TiO_2 NTs under visible light. Mater Lett 143:116–119

[10] Tomaszek R, Pawlowski L, Gengembre L, Laureyns J, Znamirowski Z, Zdanowski J (2006) Microstructural characterization of plasma sprayed TiO_2 functional coating with gradient of crystal grain size. Surf Coat Technol 201:45–56

[11] Shi P, Ng WF, Wong MH, Cheng FT (2009) Improvement of corrosion resistance of pure magnesium in Hanks' solution by microarc oxidation with sol–gel TiO_2 sealing. J Alloy Compd 469:286–292

[12] Santillan MJ, Quaranta N, Boccaccini AR (2010) Titania and titania–silver nanocomposite coatings grown by electrophoretic deposition from aqueous suspensions. Surf Coat Technol 205:2562–2571

[13] Sun Y, Zhitomirsky I (2012) Electrophoretic deposition of titanium dioxide using organic acids as charging additives. Mater Lett 73:190–193

[14] Tang F, Uchikoshi T, Ozawa K, Sakka Y (2006) Effect of polyethylenimine on the dispersion and electrophoretic deposition of nano-sized titania aqueous suspensions. J Eur Ceram Soc 26:1555–1560

[15] Besra L, Uchikoshi T, Suzuki TS, Sakka Y (2008) Bubble-free aqueous electrophoretic deposition (EPD) by pulse-potential application. J Am Ceram Soc 91:3154

[16] Laamari M, Ben Youssef A, Bousselmi L (2016) TiO_2 photoanodes developed by cathodic electrophoretic deposition in aqueous media: effect of the applied voltage. J Adv Oxid Technol 19:165–170

[17] Laamari M, Ben Youssef A, Bousselmi L (2016) TiO_2 electrophoretic deposition of titanium dioxide films on cooper in aqueous media. Water Sci Technol 74(2):424–430

[18] Besra L, Liu M (2007) A review on fundamentals and applications of electrophoretic deposition (EPD). Prog Mater Sci 52:1–61

[19] Wang S, Huang B (2008) Field emission properties of Ag/SiO_2/carbon nanotube films by pulsed voltage co-electrophoretic deposition. Thin Solid Film 517:1245–1250

[20] Naim MN, Kuwata M, Kamiya H, Lenggoro IW (2009) Deposition of TiO_2 nanoparticles in surfactant-containing aqueous suspension by a pulsed DC charging-mode electrophoresis. J Ceram Soc Jpn 117:127–132

[21] Naim MN, Kuwata M, Kamiya H, Lenggoro IW (2010) Electrophoretic packing structure from aqueous nanoparticle suspension in pulse DC charging. Colloids Surf A 360:13–19

[22] Santillán MJ, Membrives F, Quaranta N, Boccaccini AR (2008) Characterization of TiO_2 nanoparticle suspensions for electrophoretic deposition. J Nanopart Res 10:787

[23] Lin CK, Yang TJ, Feng YC, Tsung TT, Su CY (2006) Characterization of elecrophoretically deposited nanocrystalline titanium dioxide films. Surf Coat Technol 200:3184

[24] Dor S, Rühle S, Ofir S, Adler M, Grinis L, Zaban A (2009) The influence of suspension composition and deposition mode on the electrophoretic deposition of TiO_2 nanoparticle agglomerates. Colloids Surf A 342(1–3):70

[25] Tan W, Yin X, Zhou X, Zhang J, Xiao X, Lin Y (2009) Electrophoretic deposition of nanocrystalline TiO_2 films on Ti substrates for use in flexible dye-sensitized solar cells. Electrochim Chem Acta 54(19):4467–4472

[26] Lebrette S, Pagnoux C, Abélard P (2004) Stability of aqueous TiO_2 suspensions: influence of ethanol. J Colloid Interface Sci 280:400

[27] Lebrette S, Pagnoux C, Abélard P (2006) Fabrication of titania dense layers by electrophoretic deposition in aqueous media. J Eur Ceram Soc 26:2727

[28] Hanaor D, Michelazzi M, Veronesi P, Leonelli C, Romagnoli M, Sorrell C (2011) Anodic aqueous electrophoretic deposition of titanium dioxide using carboxylic acids as dispersing agents. J Eur Ceram Soc 31:1041–1047

[29] Shan CX, Hou X, Choy KL (2008) Corrosion resistance of TiO_2 films grown on stainless steel by atomic layer deposition. Surf Coat Technol 202:2399–2402

[30] Krishna DSR, Sun Y, Chena Z (2011) Magnetron sputtered TiO_2 films on a stainless steel substrate: Selective rutile phase formation and its tribological and anti-corrosion performance. Thin Solid Films 519:4860–4864

[31] Ribeiro R, Sousa M, Araújo FO, Costa JAP, Nishimoto A, Viana BC, Jr, Alves C (2016) Deposition of TiO_2 film on duplex stainless steel substrate using the cathodic cage plasma technique. Mater Res 19:1207–1212

[32] Foruzanmehr M, Hosainalipour SM, Tehrani SM, Aghaeipour M (2014) Nano-structure TiO_2 film coating on 316L stainless steel via sol-gel technique for blood compatibility Improvement. Nanomed J 1:128–136

[33] Nurhayati E, Yang H, Chen C, Liu C, Juang Y, Huang C, Hu C (2016) Electro-photocatalytic fenton decolorization of orange G using mesoporous TiO_2/stainless steel mesh photo-electrode prepared by the sol-gel dip-coating method. Int J Electrochem Sci 11:3615–3632

[34] Bamoulid L, Maurette MT, De Caro D, Beb Bachir A, Aries L, El Hajjaji S, Benoît-Marquié F, Ansart F (2008) An efficient protection of stainless steel against corrosion: combination of a conversion layer and titanium dioxide deposit. J Surf Coat Technol 202:520–5026

[35] You X, Chen F, Zhang J (2005) Effects of calcination on the physical and photocatalytic properties of TiO_2 powders prepared by sol-gel template method. J Sol Gel Sci Technol 34:181–187

[36] Moser J, Gratzel M (1982) Photochemistry with colloidal semiconductors. Laser studies of halide oxidation in colloidal dispersions of TiO_2 and α-Fe_2O_3. Helv Chim Acta 65:1436–1444

[37] Moser J, Gratzel M (1983) Light-induced electron transfer in colloidal semiconductor dispersions: single vs. dielectronic reduction of acceptors by conduction-band electrons. J Am Chem Soc 105:6547–6555

[38] Cordero-Arias L, Cabanas-Polo S, Gilabert J, Goudouri OM, Sanchez E, Virtanen S, Boccaccini AR (2014) Electrophoretic deposition of nanostructured TiO_2/alginate and TiO_2-bioactive glass/alginate composite coatings on stainless steel. Adv Appl Ceram 113:42–49

[39] Bakardjieva S, Stengl V, Szatmary L, Subrt J, Lukac J, Murafa N, Niznansky D, Cizek K, Jirkovsky J, Petrova N (2006) Transformation of brookite-type TiO_2 nanocrystals to

rutile: correlation between microstructure and photoactivity. J Mater Chem 16:1709–1716

[40] Ipaz L, Caicedo JC, Esteve J, Espinoza-Beltran FJ, Zambrano G (2012) Improvement of mechanical and tribological properties in steel surfaces by using titanium–aluminium/20 titanium–aluminium nitride multilayered system. Appl Surf Sci 258:3805–3814

[41] Maleki SA, Mirzaeia M, Azimia A (2015) COD reduction by TiO_2/graphene photocatalytic treatment of ethylene dichloride in wastewater. Desalin Water Treat 57:13207–13212

[42] Hsu HC, Cheng CS, Chang CC, Yang S, Chang CS, Hsieh WF (2005) Orientation-enhanced growth and optical properties of ZnO nanowires grown on porous silicon substrates. Nanotechnology 16:297–301

[43] Boukhachem A, Ouni B, Karyaoui M, Madani A, Chtourou R, Amlouk M (2012) Structural, opto-thermal and electrical properties of ZnO: Mo sprayed thin films. Mater Sci Semicond Process 15:282–292

[44] Zhang H, Banfield JF (2000) Understanding polymorphic phase transformation behavior during growth of nanocrystalline aggregates: insights from TiO_2. J Phys Chem B 104:3481–3487

[45] Li W, Ni C, Lin H, Huang CP, Ismat Shah S (2004) Size dependence of thermal stability of TiO_2 nanoparticles. J Appl Phys 96:6663

[46] Zhang WF, He YL, Zhang MS, Yin Z, Chen Q (2000) Raman scattering study on anatase TiO_2 nanocrystals. J Phys D Appl Phys 33:912

[47] Zhang J, Li M, Feng Z, Chen J, Li C (2006) UV raman spectroscopic study on TiO_2. I. Phase transformation at the surface and in the bulk. J Phys Chem 110:927

[48] Wang L, Egerton T (2012) The effect of transition metal on the optical properties and photoactivity of nano-particulate titanium dioxide. J Mater Science Res 1:19–27. https://doi.org/10.5539/jmsr.v1n4p19

[49] Ould-Chikh S, Proux O, Afanasiev P, Khrouz L, Hedhili MN, Anjum DH, Harb M, Geantet C, Basset JM, Puzenat E (2014) Photocatalysis with chromium-doped TiO_2: bulk and surface doping. Chemsuschem 7:1361–1371

[50] Zhu J, Chen F, Zhang J, Chen H, Anpo M (2006) Fe^{3+}–TiO_2 photocatalysts prepared by combining sol–gel method with hydrothermal treatment and their characterization. J Photochem Photobiol, A 18:196–204

[51] Zhu J, Zheng W, He B, Zhang J, Anpo M (2004) Characterization of Fe–TiO_2 photocatalysts synthesized by hydrothermal method and their photocatalytic reactivity for photodegradation of XRG dye diluted in water. J Mol Catal A: Chem 216:35–43

[52] Yung LC, Fei CC, Mandeep JC, Amin N, Laic KW (2015) Bulk substrate porosity verification by applying Monte Carlo modeling and Castaing's formula using energy-dispersive X-rays. J Electron Imaging 24:061105

[53] El-Hossary FM, Negm NZ, Khalil SM, Abed El-Rahman AM, Raaif M, Mändl S (2010) Effect of annealing temperature on hardness, thickness and phase structure of carbonitrided 304 stainless steel. Appl Phys A 99:489–495

[54] Yoo DJ, Tamaki J, Park SJ, Miura N, Yamazoe N (1995) Effects of thickness and calcination temperature on tin dioxide sol-derived thin-film senso. J Electrochem Soc 142:105–107

[55] Mechiakh R, Ben Sedrine N, Ben Naceur J, Chtourou R (2011) Elaboration and characterization of nanocrystalline TiO_2 thin films prepared by sol–gel dip-coating. Surf Coat Technol 206(2–3):243–249

[56] Bakri AS, Sahdan MZ, Adriyanto FN, Raship NA, Said NDM, Abdullah SA, Rahim MS (2017) Effect of annealing temperature of titanium dioxide thin films on structural and electrical properties. Am Inst Phys 1788:030030

[57] Kim KD, Pfadler T, Zimmermann E, Feng Y, Dorman JA, Weickert J, Schmidt-Mende L (2015) Decoupling optical and electronic optimization of organic solar cells using high performance temperature-stable TiO_2/Ag/TiO_2 electrodes. Appl Mater 3:106105

[58] Sedghi A, Miankushki HN (2015) The effect of drying and thickness of TiO_2 electrodes on the photovoltaic performance of dye-sensitized solar cells. Int J Electrochem Sci 10:3354–3362

[59] Domtau DL, Simiyu J, Ayieta EO, Muthoka B, Mwabora JM (2016) Optical and electrical properties dependence on thickness of screen-printed TiO_2 thin films. J Mater Phys Chem 4:1–3

[60] Gaillard Y, Rico YJ, Jimenez-Pique E, González-Elipe AR (2009) Nanoindentation of TiO_2 thin films with different microstructures. J Phys D Appl Phys 42(14):145305–145314

[61] Yaghoubi H, Taghavinia N, Keshavarz Alamdari E, Volinsky AA (2010) Nanomechanical properties of TiO_2 granular thin films. ACS Appl Mater Interfaces 2(9):2629–2636

[62] Dukhyun C, Sangmin L, Changwoo L, Pyungsoo L, Junghyun L, Kunhong L, Hyunchul P, Woonbong H (2007) Dependence of the mechanical properties of nanohoneycomb structures on porosity. J Micromech Microeng 17:501

[63] Sanders PG, Eastman JA, Weertman JR (1997) Elastic and tensile behavior of nanocrystalline copper and palladium. Acta Mater 45:4019–4025

[64] Vaz F, Machado P, Rebouta L, Cerqueira P, Goudeau PH, Rivière JP, Alves E, Pischow K, Rijk J (2003) Mechanical characterization of reactively magnetron-sputtered TiN films. Surf Coat Technol 174–175:375–382

[65] Oliver WC, Pharr GM (1992) An improved technique for determining hardness and elastic modulus using load and

displacement sensing indentation experiments. J Mater Res 7:1564

[66] Yu J, Zhao X, Yu JC, Zhong G, Han J, Zhao Q (2001) The grain size and surface hydroxyl content of superhydrophilic TiO_2/SiO_2 composite nanometer thin films. J Mater Sci Lett 20:1745–1748

[67] Sirghi L (2016) Plasma synthesis of photocatalytic TiO_x thin films. Plasma Sources Sci Technol 25:33003–33016

[68] Kobayashi T, Konishi S (2015) TiO_2 patterns with wide photo-induced wettability change by a combination of reactive sputtering process and surface modification in a microfluidic channel. J Micromech Microeng 25:115014–115026

[69] Kolouch A, Horáková M, Hájková P, Heyduková E, Exnar P, Apatenka P (2006) Relationship between photocatalytic activity, hydrophilicity and photoelectric properties of TiO_2 thin films. Probl At Sci Technol 6:198–200

[70] Mathew S, Amit KP, Thomas B, Rakesh PP, Misha H, Libish TM, Radhakrishnan P, Nampoori VP, Vallabhan CP (2012) UV-visible photoluminescence of TiO_2 nanoparticles prepared by hydrothermal method. J Fluoresc 22:1563

[71] Mattioli G, Filippone F, Alippi P, Bonapasta AM (2008) Ab initio study of the electronic states induced by oxygen vacancies in rutile and anatase TiO_2. Phys Rev B 78:241201-1–241201-4

[72] Zhou J, Zhang Y, Zhao XS, Ray AK (2006) Photodegradation of benzoic acid over metal-doped TiO_2. Ind Eng Chem Res 45:3503

[73] Liu B, Zhao X, Zhang N, Zhao Q, He X, Feng J (2005) Photocatalytic mechanism of TiO_2–CeO_2 films prepared by magnetron sputtering under UV and visible light. Surf Sci 595:203

[74] Liu B, Wen L, Zhao X (2007) The photoluminescence spectroscopic study of anatase TiO_2 prepared by magnetron sputtering. Mater Chem Phys 106:350

[75] Chang CH, Liu CH, Chen C, Cheng HE, Luc TC (2012) The differences in optical characteristics of TiO_2 and TiO_2/AAO nanotube arrays fabricated by atomic layer deposition. J Electrochem Soc 159:136–140

[76] Preclikova J, Galar P, Trojanek F, Danis S, Rezek B, Gregora I, Němcová Y, Malý P (2010) Nanocrystalline titanium dioxide films: influence of ambient conditions on surface and volume related photoluminescence. J Appl Phys 108:113502

[77] Liu J, Li J, Sedhain A, Lin J, Jiang H (2008) Structure and photoluminescence study of TiO_2 nanoneedle texture along vertically aligned carbon nanofiber arrays. J Phys Chem C 112:17127

[78] Sadeghzadeh-Attar A (2016) Structural and optical characteristic of single crystal rutile–titania nanowire arrays prepared in alumina membranes. Mater Chem Phys 1–7

[79] Klubnuan S, Suwanboon S, Amornpitoksuk P (2016) Effects of optical band gap energy, band tail energy and particle shape on photocatalytic activities of different ZnO nanostructures prepared by a hydrothermal method. Opt Mater 53:134–141

[80] Yu JG, Yu HG, Cheng B, Zhao XJ, Yu JC, Ho WK (2003) The effect of calcination temperature on the surface microstructure and photocatalytic activity of TiO_2 thin films prepared by liquid phase deposition. J Phys Chem B 107:13871–13879

[81] Rashed MN, El-Amin ZZ (2007) Photocatalytic degradation of methyl orange in aqueous TiO_2 under different solar irradiation sources. Int J Phys Sci 2:73

[82] Linsebigler AL, Lu G, Yates JT (1995) Photocatalysis on TiO_2 surfaces: principles, mechanisms, and selected results. Chem Rev 95:735

[83] Liu H, Cheng S, Wu M, Wu H, Zhang J, Li W, Cao C (2000) Photoelectrocatalytic degradation of sulfosalicylic acid and its electrochemical impedance spectroscopy investigation. J Phys Chem A 104:7016–7020

[84] Banisharif A, Khodadadi AA, Mortazavi Y, Firooz AA, Beheshtian J, Agaha S, Menbari S (2015) Highly active Fe_2O_3-doped TiO_2 photocatalyst for degradation of trichloroethylene in air under UV and visible light irradiation: experimental and computational studies. Appl Catal B 165:209–221

[85] Wang M, Pyeon M, Gönüllü Y, Kaouk A, Shen S, Guo L, Mathur S (2015) Constructing Fe_2O_3/TiO_2 core-shell photoelectrodes for efficient photoelectrochemical water splitting. Nanoscale 7(22):10094–10100

[86] Noh E, Noh KJ, Yun KS, Kim BR, Jeonh HJ, Oh HJ, Jung SC, Kang WS, Kim SJ (2013) Enhanced water splitting by Fe_2O_3–TiO_2–FTO photoanode with modified energy band structure. Sci World J 2013:723201–723209

[87] Shinde SS, Bhosale CH, Rajpure KY (2011) Photocatalytic oxidation of salicylic acid and 4-chlorophenol in aqueous solutions mediated by modified $AlFe_2O_3$ catalyst under sunlight. J Mol Catal A: Chem 347:65–72

[88] Fateh R, Dillert R, Bahnemann DW (2014) Self-cleaning properties, mechanical stability, and adhesion strength of transparent photocatalytic TiO_2-ZnO coatings on polycarbonate. Appl Mater Interfaces 6:2270–2278

[89] Çomakl O, Yetim T, Çelik A (2014) The effect of calcination temperatures on wear properties of TiO_2 coated CP-Ti. Surf Coat Technol 246:34–39

[90] Lackner JM, Waldhauser W, Ebner R, Major B, Schoberl T (2004) Pulsed laser deposition of titanium oxide coatings at room temperature-structural, mechanical and tribological properties. Surf Coat Technol 180–181:585–590

[91] Bendavid A, Martin PJ, Takikawa H (2000) Deposition and modification of titanium dioxide thin films by filtered arc deposition. Thin Solid Films 360:241–249

[92] Kern P, Schwaller P, Michler J (2006) Electrolytic deposition of titania films as interference coatings on biomedical implants: microstructure, chemistry and nano-mechanical properties. Thin Solid Films 494:279–286

[93] Sun T (2004) Tribological rutile-TiO_2 coating on aluminium alloy. Appl Surf Sci 233:328–335